

PFC/JA-94-36

**Scaling and Transport Analysis of Divertor
Conditions on the Alcator C-Mod Tokamak**

B. LaBombard, J. Goetz, C. Kurz, D. Jablonski, B. Lipschultz,
G. McCracken, A. Niemczewski, R.L. Boivin, F. Bombarda¹,
C. Christensen, S. Fairfax², C. Fiore, D. Garnier, M. Graf,
S. Golovato, R. Granetz, M. Greenwald, S. Horne,
A. Hubbard, I. Hutchinson, J. Irby, J. Kesner, T. Luke,
E. Marmor, M. May³, P. O'Shea, M. Porkolab, J. Reardon,
J. Rice, J. Schachter, J. Snipes, P. Stek, Y. Takase,
J. Terry, G. Tinios, R. Watterson, B. Welch⁴, S. Wolfe

November 1994

¹ENEA-Frascati, Frascati, Italy.

²Now at Failure Analysis Associates, Inc., Cambridge, MA.

³Johns Hopkins University, Baltimore, Md., USA

⁴University of Maryland, College Park, Md., USA

Submitted to Physics of Plasmas.

This work was supported by the U. S. Department of Energy Contract No. DE-AC02-78ET51013. Reproduction, translation, publication, use and disposal, in whole or in part by or for the United States government is permitted.

Scaling and Transport Analysis of Divertor Conditions on the Alcator C-Mod Tokamak

B. LaBombard, J. Goetz, C. Kurz, D. Jablonski, B. Lipschultz, G. McCracken, A. Niemczewski, R. L. Boivin, F. Bombarda ^{a)}, C. Christensen, S. Fairfax ^{b)}, C. Fiore, D. Garnier, M. Graf, S. Golovato, R. Granetz, M. Greenwald, S. Horne, A. Hubbard, I. Hutchinson, J. Irby, J. Kesner, T. Luke, E. Marmar, M. May ^{c)}, P. O'Shea, M. Porkolab, J. Reardon, J. Rice, J. Schachter, J. Snipes, P. Stek, Y. Takase, J. Terry, G. Tinios, R. Watterson, B. Welch ^{d)}, S. Wolfe

Plasma Fusion Center
Massachusetts Institute of Technology
Cambridge, MA 02139, USA

Detailed measurements and transport analysis of divertor conditions in Alcator C-Mod [Phys. Plasmas **1**, 1511 (1994)] are presented for a range of line-averaged densities, $0.7 < \bar{n}_e < 2.2 \times 10^{20} \text{ m}^{-3}$. Three parallel heat transport regimes are evident in the scrape-off layer: sheath-limited conduction, high-recycling divertor and detached divertor, which can coexist in the same discharge. Local cross-field pressure gradients are found to scale simply with local electron temperature. This scaling is consistent with classical electron parallel conduction being balanced by anomalous cross-field transport ($\chi_{\perp} \sim 0.1 \text{ m}^2 \text{ s}^{-1}$) proportional to the local pressure gradient. 60 to 80% of divertor power is radiated in attached discharges, approaching 100% in detached discharges. Detachment occurs when the heat flux to the plate is low and the plasma pressure is high ($T_e \sim 5 \text{ eV}$). High neutral pressures in the divertor are nearly always present (1 - 20 mTorr), sufficient to remove parallel momentum via ion-neutral collisions.

a) ENEA Frascati, Italy.

b) Now at Failure Analysis Associates, Inc., Cambridge, MA.

c) Johns Hopkins University.

d) University of Maryland.

I. Introduction

The design of a successful divertor for a fusion reactor such as ITER requires the ability to accurately predict and control the plasma conditions there. Yet, owing to the turbulent particle and heat transport in the boundary layer, it is not possible to compute from first principles the profile of heat and particle fluxes, for example, to the divertor surfaces. Experiments in existing tokamaks are therefore critically needed to shed light on the transport processes active in the divertor, the scaling of divertor conditions with core plasma conditions and the dependence of divertor conditions on other controllable parameters such as divertor geometry, impurity concentrations, and neutral gas pressures. It is further hoped that the compilation of such an empirical database will elucidate the dominant transport processes active in the divertor/edge plasma and enable more robust physics-based scaling models to be developed.

Alcator C-Mod¹ is in a unique position to explore divertor and edge physics phenomena with an unprecedented combination of control parameters: high magnetic field ($B > 5$ tesla), high SOL power density, ($q_{//sol} > 200$ MW m⁻², currently with ohmic heating alone), high divertor plasma density ($n_{div} > 5 \times 10^{20}$ m⁻³), shaped divertor geometry, and a metal (Mo) divertor and first-wall. An extensive array of diagnostics has been assembled for divertor studies.² This paper reports the first results of a series of experiments aimed at characterizing the parallel and perpendicular heat transport mechanisms and their scalings in the divertor and scrape-off layer (SOL). The focus of the present study is on single-null, ohmically heated, diverted discharges, with core plasma density (\bar{n}_e) as the principal control parameter.

Section II describes the divertor geometry and arrangement of diagnostics. Measurements of SOL and divertor plasma profiles are presented in Sec. III. In section IV, heat transport in the divertor and scrape-

off layer is discussed with the help of a simplified transport model. Section V briefly describes SOL and divertor conditions leading to plasma detachment.

II. Experimental Arrangement

The geometry of the divertor and the arrangement of key divertor diagnostics for these studies is shown in Fig. 1. Detailed information on Alcator C-Mod's design, diagnostics, and operational characteristics can be found elsewhere.¹ Molybdenum probes are mounted on both the inner and outer divertor plates at 16 poloidal locations. The probes extend 0.5 mm beyond the surface of the divertor, presenting a domed surface to the plasma flux. This geometry avoids problems associated with the interpretation of probe characteristics at small oblique field line angles.³ Data from the outer divertor probe array was used for the present studies.

A fast-scanning Langmuir probe is used to record SOL plasma profiles up to the last closed flux surface (LCFS) at a position 'upstream' from the entrance to the divertor. The probe head consists of a 15 mm diameter molybdenum body with four Langmuir probe elements. The probe elements have directional sensitivity (along and across B) and maintain a field line grazing angle of about 20 degrees. Densities and temperatures along the probe's trajectory are obtained by fitting positive and negative-going I-V characteristics generated by a 500 Hz voltage sweep.

Data from both the divertor probe array and the fast-scanning probe are mapped onto magnetic flux surfaces reconstructed from magnetic measurements⁴ and the EFIT plasma equilibrium code.⁵ Flux surfaces in the scrape-off layer are labeled by the coordinate, ρ , which is defined as the distance in major radius from the last-closed flux surface at the outboard mid-plane. A good match is obtained between the pressure profiles from the two diagnostics by adjusting the scanning probe +1 mm in ρ (relative to

EFIT mapping) and the divertor array -1 mm. This level of error is within the expected accuracy of the EFIT reconstruction and the positioning accuracy of the scanning probe.

Radiated power in the plasma core and divertor regions is monitored by a system of 4 bolometer arrays.⁶ Figure 1 shows the views of the outer 'ledge' bolometer array which is found to provide a good measurement of the total radiation in the divertor and near the x-point.

Neutral gas pressures are monitored in the private flux region of the divertor using a combination of fast-response in-situ ionization gauges (shown behind the divertor in Fig.1) and a slower response shielded ionization gauge at the bottom of a vertical port.⁷

The present experiments were conducted in ohmically heated, single-null diverted deuterium plasmas with central conditions of $B_T = 5.3$ tesla, plasma current $0.7 < I_p < 0.8$ MA, line-averaged density $0.7 < \bar{n}_e < 2.2 \times 10^{20} \text{ m}^{-3}$, and vertical elongation of 1.6. The goal was to study the edge plasma behavior in discharges with nearly identical plasma current, ohmic input power, and magnetic equilibrium while varying the core density over a factor of 3.

Figure 2 shows representative time traces of plasma current, line-average density and divertor/edge probe signals during the steady-state portion of a discharge. The scanning probe position (in flux surface coordinate, ρ) and current collection traces show two insertion times: one before a detached divertor plasma event occurring at 0.82 seconds and one during detached divertor operation. The modulation in the current signal from probe 6 (typical of all probes in the array) is in response to a 50 Hz voltage bias waveform (positive signal indicates ion collection). Complete plasma density and temperatures across the divertor surface are deduced at roughly 10 msec intervals by fitting current-voltage characteristics using

standard magnetized probe theory. The time evolution of density and temperature on probe 6 is shown in the figure as an example.

III. SOL and Divertor Conditions

A. Cross-Field Temperature and Density Profiles

Typical cross-field profiles of density and electron temperature deduced from a single insertion of the scanning probe are shown in Fig. 3. Data from the four separate sensors on the probe head overlay reasonably well for both insertion and retraction. One may note a systematic variation between the densities deduced from the 'east' and 'west' probes, indicating a plasma flow along the magnetic field and/or a toroidal rotation that varies with the cross-field coordinate. However, discussions of these observations are beyond the scope of the present paper.

In order to facilitate a comparison of density and temperature profiles between different discharges, a smooth spline curve was fitted to data from each probe scan, as is shown in Fig.3. This averaging process takes advantage of the good statistics generated from four independent probe sensors scanning in and out. The averaging process also minimizes the impact of plasma flows on the local density estimate since the 'upstream' and 'downstream' unidirectional probes are effectively summed together to form a single bi-directional probe.

Figure 4 displays fitted SOL profiles of density, temperature, and electron pressure as the core plasma density is systematically varied. A number of important observations are summarized by this figure: (1) All profiles display a non-exponential dependence on flux surface coordinate, ρ , i.e., the slope on a logarithmic plot varies substantially with ρ . For the case of electron pressure, the local gradient scale length (e-folding length) can vary by as much as a factor of ~ 4 going from 2-3 mm near the separatrix to 12 mm at a location of $\rho \approx 15$ mm. (2) All local gradient scale lengths appear

to depend on the plasma density, having the smallest values at low density and largest values at high density. (3) The density profile exhibits shorter gradient scale lengths than the temperature profile near the separatrix and the gradient there appears to be most strongly dependent on the central density.

B. Parallel Temperature and Density Gradients

Plasma conditions at the divertor plate surface can be directly compared to those measured 'upstream' on the same flux surfaces by the scanning probe. Figure 5 shows electron pressure and temperature profiles from the two probe diagnostics for three values of central line-averaged density. The electron pressure at the divertor plate is multiplied by a factor of 2 to account for the sound-speed flow there.

Three regimes of parallel plasma transport to the divertor surface can clearly be identified that depend not only on the central density in these discharges but also on the flux surface location:

1 -- Profiles at low density, $\bar{n}_e < 10^{20} \text{ m}^{-3}$, exhibit an electron temperature that is nearly constant along the magnetic field lines for $\rho > 5$ mm. Electron pressure is also constant along \mathbf{B} and the divertor sheath appears to support all of the temperature drop on these flux tubes. Electron temperatures everywhere are the hottest in the low density regime.

2 -- Profiles at moderate density, $1.0 < \bar{n}_e < 1.8 \times 10^{20} \text{ m}^{-3}$, show a 'high recycling' divertor condition across the profile: the electron temperature falls at the divertor plate relative to 'upstream' while the density rises there so as to keep pressure approximately constant along \mathbf{B} . A temperature gradient arises along the field line presumably because parallel electron thermal conduction is poorer at lower temperatures ($\kappa \propto T^{5/2}$), while the divertor sheath temperature can remain low since it conducts heat more readily at the higher densities. The high recycling condition is seen in

portions of the other profiles also: near the separatrix in the low density case and at large values of ρ in the highest density case.

3 -- Profiles at high density, $\bar{n}_e > 1.8 \times 10^{20} \text{ m}^{-3}$, show a 'detached divertor' condition over some portion of the profile. Both the divertor electron temperature and the plasma density are very low in this regime, clearly violating constant pressure along B.

C. Scaling of Parallel Gradients with \bar{n}_e

Figure 6 shows the evolution with \bar{n}_e of electron pressure, temperature, and density at the divertor surface and 'upstream' at the scanning probe location for the $\rho = 4$ flux surface. The 'sheath-limited', 'high recycling', and 'detached divertor' regimes are clearly evident as \bar{n}_e is varied. Electron pressure maps fairly well between the two probe diagnostics up to divertor detachment. The electron temperature at the divertor plate decreases uniformly with increasing \bar{n}_e . Divertor detachment occurs when the electron temperature at the divertor plate is at or below a level of ~ 5 eV. In the high-recycling regime, the density at the divertor plate shows a nonlinear scaling with core density, similar to that expected from standard two-point model analyses. In this regime, the divertor density is often observed to exceed the central line-averaged density.

IV. Transport Analysis

A quantitative comparison can be made between the experimental observations and a heat transport model that balances anomalous perpendicular transport with classical electron parallel conduction, sheath-limited heat flow, and divertor radiation.

A. Model for Parallel Heat Transport and Divertor Radiation

Conservation of energy in this model requires

$$\nabla_{//} \cdot \mathbf{q}_{//} + \nabla_{\perp} \cdot \mathbf{q}_{\perp} + Q_{\text{Rad}} = 0 \quad (1)$$

while $\mathbf{q}_{//}$ in the bulk plasma is $\mathbf{q}_{//} \cong -\frac{2}{7} \kappa_0 \nabla_{//} T^{7/2}$ and at the sheath is

$$\mathbf{q}_{//} \Big|_{\text{sheath}} = e \gamma n_d T_d^{3/2} \sqrt{\frac{2e}{m_i}} \cdot \quad (2)$$

Here, κ_0 is $2.8 \times 10^3 \text{ W m}^{-1} \text{ eV}^{-7/2}$, e is $1.6 \times 10^{-19} \text{ J eV}^{-1}$, γ is the sheath heat transfer coefficient, and subscripts 'd' refer to conditions at the divertor plate.

Now consider the edge plasma to be composed of a series of adjacent flux tubes each with separate length S_d , extending from the symmetry point, $S=0$, to the divertor surface, $S=S_d$. Integrating Eq. (1) over the length of a given flux tube,

$$\mathbf{q}_{//} \Big|_{\text{sheath}} = -\langle \nabla_{\perp} \cdot \mathbf{q}_{\perp} \rangle S'_d - \int_0^{S_d} Q_{\text{Rad}} \partial S = -(1-f_{\text{Rad}}) \langle \nabla_{\perp} \cdot \mathbf{q}_{\perp} \rangle S'_d \quad (3)$$

where f_{Rad} is defined as the fraction of total power into the flux tube that is radiated rather than conducted to the sheath and $\langle \nabla_{\perp} \cdot \mathbf{q}_{\perp} \rangle$ represents an average value along the flux tube's length over a distance S'_d . S'_d is loosely defined as the length of the flux tube outside the divertor region. This formulation accounts for the fact that the magnitude of $\nabla_{\perp} \cdot \mathbf{q}_{\perp}$ is much smaller in the divertor since the core plasma - SOL plasma interface changes to a private flux - common flux SOL plasma interface there.

The temperature upstream from the divertor can be obtained from integrating Eq. (1) twice and by assuming a model profile for the distribution of divertor radiation along the length of the flux tube. The upstream temperature is insensitive to the spatial distribution of the radiation, as long as the radiation is localized to the divertor. Assuming that the radiation emissivity decreases with a parallel decay length of λ_R ,

$$Q_{\text{Rad}} = Q_0 e^{(S - S_d)/\lambda_R}, \quad (4)$$

the upstream temperature is

$$T^{7/2} = T_d^{7/2} - \frac{7}{4K_0} \langle \nabla_{\perp} \cdot \mathbf{q}_{\perp} \rangle S_d'^2 \quad (5)$$

$$\times \left\{ \frac{2S_d}{S_d'} - 1 - \frac{2S_d^2}{S_d'^2} - \frac{f_{\text{Rad}} 2\lambda_R}{(1 - e^{-S_d/\lambda_R}) S_d'} \left[1 + \frac{S - S_d}{\lambda_R} e^{-S_d/\lambda_R} - e^{(S - S_d)/\lambda_R} \right] \right\}.$$

This expression is valid for $S < S_d'$. Typical values of S_d , S_d' , and S at the scanning probe location for the discharges studied here are 12, 10, and 7 meters, respectively. The bracketed term in Eq. (5) is of order unity for S corresponding to the scanning probe location. The upstream temperature at this location is a weak function of f_{Rad} and λ_R for $\lambda_R < S_d$. In the remaining analysis, λ_R is approximated as $\lambda_R \cong 0.2 S_d$.

B. Model for Cross-Field Heat Transport

Local cross-field fluxes are often modeled to be diffusive, proportional to the local density and temperature gradients. Adopting this strategy and assuming that $\chi_{\perp}^i \cong \chi_{\perp}^e$, the cross field heat flux can be written as the sum of conduction and convection terms,

$$\mathbf{q}_{\perp} = \mathbf{q}_{\perp}^i + \mathbf{q}_{\perp}^e = -\chi_{\perp} n \nabla_{\perp} (T_i + T_e) + \frac{5}{2} (T_i + T_e) D_{\perp} \nabla_{\perp} n. \quad (6)$$

It is mathematically convenient to assume that particle and heat diffusivity satisfy $D_{\perp} \cong \frac{2}{5} \chi_{\perp}$ and that $T_i \approx T_e$. In this case,

$$\nabla_{\perp} \cdot \mathbf{q}_{\perp} \cong -4 \nabla_{\perp} \cdot \chi_{\perp} \nabla_{\perp} n T_e. \quad (7)$$

Equivalently, one could just postulate from the outset that the cross-field heat flux in the SOL is to be modeled as a flux proportional to the local pressure gradient. The deduced values of χ_{\perp} in this case would be a factor of 2 larger.

The advantage of modeling the cross-field transport by Eq. (7) is readily apparent. Assuming that plasma pressure is constant on a flux

surface, measurements of the pressure gradients at the scanning probe location can be suitably averaged over magnetic flux surfaces to determine the $\langle \nabla_{\perp} \cdot \mathbf{q}_{\perp} \rangle$ term in Eq. (5) for a given flux tube.

C. Comparison with Experiment

Equations (5) and (7) imply that in the high-recycling regime the local pressure gradient scale length at the scanning probe location, λ_p , should scale with the upstream electron temperature, the electron pressure on the flux surface, and the average value of χ_{\perp} on the flux surface. The effect of χ_{\perp} varying across flux surfaces can be crudely considered by postulating $\chi_{\perp} \cong \chi_{0\perp} (n T_e)^{\alpha}$. Approximating $\nabla_{\perp}^2 n T_e \cong n T_e / \lambda_p^2$, the transport model implies

$$\lambda_p \cong S'_d \left(\frac{7 e (\alpha + 1) \chi_{0\perp}}{\kappa_0} \right)^{1/2} n^{(\alpha + 1)/2} T_e^{(2\alpha - 5)/4} \quad (8)$$

with the restriction that $\alpha > -1$. The values n and T_e refer to conditions 'upstream' near the scanning probe location. For values of α less than about -1 , we expect to see a fairly strong inverse relationship between the local pressure e-folding length and the local electron temperature. The data does indeed show this behavior.

Figure 7 plots local electron pressure e-folding length versus the local electron temperature recorded by the scanning probe. Data points on this plot were obtained from 23 probe scans in discharges with densities ranging from $0.8 < \bar{n}_e < 2.2 \times 10^{20} \text{ m}^{-3}$ under both attached and detached divertor conditions. The different symbols correspond to measurements made on different flux surfaces. The values for λ_p were determined by fitting an exponential to the pressure profile locally ($\pm 1 \text{ mm}$) about that flux surface. A curve proportional to $T^{-5/4}$ (case of $\alpha = 0$) is shown for reference.

Note that the local electron pressure e-folding lengths at all values of ρ appear to lie on the same curve which is proportional to $\sim T^{-5/4}$. For example, values for λ_p on the $\rho = 2$ mm flux surface trace out a scaling as the electron temperature there varies from 20 to 50 eV (by changing \bar{n}_e). Similarly, λ_p on the other flux surfaces trace out the same curve as the local electron temperatures change, except they are offset according to their T_e values. This observation reinforces the notion that transport depends on the local values of n and T_e and not explicitly on flux surface location.

A two-parameter regression analysis on this data set yields a slightly better fit than is shown on the figure with the proportionality $\lambda_p \propto T^{-1.56} n^{0.23}$. From Eq. (8), these exponents suggest a value of $\alpha \approx -0.5$. However, more data are needed in order to render the scaling with local density to be statistically significant. At the present time, one should treat inferences about the scaling of χ_\perp from these data with caution. A regression on T_e alone yields $\lambda_p \propto T^{-1.4}$.

Plots of local λ_n and λ_T versus local T_e also show an inverse trend with T_e . However, the scatter in the data is slightly larger for the case of λ_n and very large for λ_T .

These observations lend support to the assumptions in the simplified heat transport model: cross-field heat transport proportional to the local pressure gradient balanced by classical parallel electron heat conduction.

D. Estimates of χ_\perp

Measurements of the upstream temperature and pressure profiles, the divertor plate electron temperature, and the parallel heat flux to the divertor plate from Eq. (2) can be combined to yield estimates of both the local cross-field heat diffusivity, χ_\perp , and the fraction of the heat radiated in a given flux tube, f_{Rad} . For a specified λ_R , Eqs. (3) and (5) yield an estimate of f_{Rad} . A best-fit χ_\perp profile can then be determined by matching the $\langle \nabla_\perp \cdot \mathbf{q}_\perp \rangle$ profile

from Eq. (7) to that determined from Eq. (5). Note that the analysis does not require that the divertor remain attached. The analysis is approximately valid so long as pressure is constant on flux surfaces outside the divertor region where $\langle \nabla_{\perp} \cdot \mathbf{q}_{\perp} \rangle$ is evaluated.

At the present time, a high level of scatter in the input parameters such as $T^{7/2}$ and $\nabla_{\perp}^2 n T_e$ does not allow the spatial variation in χ_{\perp} to be reliably inferred. This is unfortunate because one might expect from the analysis above that χ_{\perp} is an increasing function of ρ (decreasing function of local plasma pressure). Fitting spatially independent $\chi_{\perp} \propto \lambda \nu \epsilon \sigma$ to the data, one finds that the error bars are quite large (>50%) for any given discharge, demonstrating the sensitivity to noise in the inputted experimental data set. Nevertheless, no obvious trend in the scaling of χ_{\perp} with \bar{n}_e was observed, even in the detached plasma cases. Typical values of χ_{\perp} are $\sim 0.1 \text{ m}^2 \text{ s}^{-1}$ over discharges with central density variation $0.8 < \bar{n}_e < 2.2 \times 10^{20} \text{ m}^{-3}$. Values of $\gamma \cong 7$ and $\lambda_R \cong 0.2 S_d$ were assumed for this analysis, although the estimated χ_{\perp} is a very weak function of these parameters.

Adopting a fixed value of $\chi_{\perp} \cong 0.1$, one can perform the inverse comparison, namely, compute $\langle \nabla_{\perp} \cdot \mathbf{q}_{\perp} \rangle$ directly from Eq. (7) and use Eq. (5) to estimate the upstream temperature at the scanning probe. f_{rad} can also be computed directly from Eq. (3). This procedure results in a very good match between the measured upstream temperature profiles ($0 \leq \rho \leq 8 \text{ mm}$) and the profiles computed from the transport model over the full range of \bar{n}_e . These findings are contrary to an analysis performed on a different set of probe data collected earlier on Alcator C-Mod⁸ and confirm the suspicion that the electron temperatures in these previous data were abnormally low. The problem has since been correlated with an electrical short-circuit to the body of the probe head and is currently under investigation.

Consistent with measurements from the divertor bolometers, the transport analysis indicates that divertor radiation is high over the entire

density range: 60 to 80% of the power in the flux tubes near the separatrix is typically radiated, approaching 100% in the detached divertor cases. Flux tubes further out in the SOL, which typically remain attached, are found to radiate a significant yet smaller fraction of their power (40-60%).

V. Divertor Detachment

Detached divertor phenomena have become the subject of recent focus in connection with developing techniques to handle the high divertor heat fluxes in ITER.⁹ As seen in the C-Mod data, detached plasmas are capable of radiating nearly 100% of the divertor heat flux. It is of interest to know the conditions under which divertor detachment occurs, the physics of detachment, and whether or not detachment can be controlled in a divertor such as in ITER. The set of experiments conducted here provides some information on the first two parts of this question. Much more work remains to be done, however.

Figure 8 displays the evolution of edge plasma parameters as the detached divertor condition is approached by varying \bar{n}_e . The parallel heat flux profile, representing the heat flux into the divertor region, is computed from the heat transport model outlined in Sec. IV. A comparison of the electron pressure upstream and at the divertor plate on the $\rho = 2$ mm flux surface indicates divertor detachment occurs at $\bar{n}_e > 1.7 \times 10^{20} \text{ m}^{-3}$ in these discharges. Also shown are electron temperature profiles across the divertor plate surface at three densities, molecular deuterium pressures behind the divertor, and the fraction of total input power radiated in the toroidal volume seen by the divertor bolometer (see Fig. (1) for geometry).

Divertor detachment typically shows up as an abrupt reduction in the ion flux to divertor probes over a portion of the divertor surface, typically at and below probe 7 on the outer divertor, and a shift in the divertor radiation to the x-point.^{1,2} Yet, the scrape-off layer conditions outside the divertor

region are seen to evolve smoothly and continuously up to and beyond the detachment threshold. A key element in achieving detachment is the increase in divertor/x-point radiation and the related decrease in parallel heat flux into the divertor as a function of increasing \bar{n}_e . Apparently, the plasma pressure rises on the divertor with \bar{n}_e until the parallel heat flux, which is monotonically falling with \bar{n}_e , can no longer support a divertor temperature greater than ~ 5 eV. During the detached state, the parallel heat flux into the divertor is at its lowest, the electron temperatures (on detached flux surfaces) are around 1-2 eV and the divertor neutral pressure is around 20 mTorr for these discharges.

The lack of any dramatic changes in the upstream conditions during the transition suggests that it is conditions localized to the divertor that precipitate the detached state. The combination of low electron temperatures and high neutral densities point to ion-neutral collisions as being responsible for the observed momentum loss along field lines. This picture of momentum loss and detachment is entirely consistent with the one originally proposed by Stangeby¹⁰ and considered in more detail by others.^{11, 12, 13, 14}

The neutral density needed to support the momentum loss can be estimated directly from the probe measurements. In the detached state, it is presumed that momentum-exchanging ion-neutral collisions dominate over ionization over a length of the field line, L , where T_e is less than 10 eV.¹⁰⁻¹⁴ In this "collision zone" the parallel flux, $\Gamma_{//}$, is approximately constant and should be equal to the measured parallel flux at the plate. The plasma pressure drop along the field line must balance the frictional drag on neutrals (charge exchange and elastic scattering):

$$\Delta P \cong L m_i \Gamma_{//} n_0 \langle \sigma v \rangle_{sc} \quad (9)$$

For the detached discharges in Fig. 8, measured values of $\Delta P \cong 4 \times 10^{21} \text{ eV m}^{-3}$, $\Gamma_{\parallel} \cong 6 \times 10^{23} \text{ m}^{-2} \text{ s}^{-1}$, along with estimates of $L \cong 2 \text{ m}$, and $\langle \sigma v \rangle_{\text{SC}} \cong 10^{-14} \text{ m}^3 \text{ s}^{-1}$, yield neutral densities, n_0 , on the order of $3 \times 10^{19} \text{ m}^{-3}$. Assuming these are predominately Franck-Condon neutrals at a few eV, the equivalent room-temperature molecular pressure in the private flux zone would be around 4 mTorr. This level of pressure is routinely achieved in the C-Mod divertor (up to 20 mTorr prior to and during detachment). Thus, it appears that there is more than sufficient neutral density in the divertor to provide a momentum cushion -- provided that the neutrals can penetrate, preferentially scatter rather than ionize, and carry the momentum to the divertor plate without a subsequent collision. In C-Mod, neutral (Frank-Condon) mean free paths are on the order of 1 cm, allowing a significant portion of the divertor fan to be affected. The local electron temperature is key to controlling this physics.

VI. Summary

Density and temperature profiles are found to exhibit clear non-exponential dependencies on the cross-field coordinate. Direct measurement of plasma density and temperature profiles 'upstream' in the common SOL and 'downstream' at the divertor plate identify three parallel heat transport regimes: sheath-limited conduction, high-recycling divertor, and detached divertor, all of which can coexist in the same discharge across the SOL profile.

Although the plasma pressure profiles exhibit complicated, non-exponential dependencies on the cross-field coordinate, it is found that the local pressure gradient scales simply with the local electron temperature. It is suggested that this scaling is a consequence of heat transport being governed by classical parallel electron conduction with cross-field transport being proportional to the cross-field pressure gradient. Anomalous cross-field heat

diffusivities on the order of $0.1 \text{ m}^2 \text{ s}^{-1}$ are found to reproduce the observed upstream temperature profiles. Radiation in the divertor as deduced from both transport analysis and divertor bolometry is found to be high in all cases: 60 to 80% of SOL power in attached discharges, approaching 100% in detached discharges.

Although the time-signature of divertor detachment is typically dramatic, i.e., a prompt reduction in the pressure on the divertor plate at an apparent threshold value of \bar{n}_e , plasma conditions outside the divertor region evolve smoothly and continuously with \bar{n}_e across the detachment threshold. Prior to and during detachment there exist sufficiently high neutral pressures in the divertor (~ 20 mTorr) to explain the observed parallel momentum loss via ion-neutral collisions - provided an ion-neutral collisional zone can be formed. The divertor is observed to detach simply when the electron temperature at the divertor plate is below ~ 5 eV - consistent with the formation of a ion-neutral collisional zone. Low divertor temperatures occur at high values of \bar{n}_e because the heat flux to the plate is low (high divertor/edge radiation) and the plasma pressure in the SOL is high.

Acknowledgments

None of these results would have been possible without the hard work, expertise, and dedication of the engineers, technical staff, students, and scientists on the Alcator team.

This work is supported by U.S. Department of Energy Contract No. DE-AC02-78ET5103.

-
- ¹I.H. Hutchinson, R. Boivin, F. Bombarda, P. Bonoli, S. Fairfax, C. Fiore, J. Goetz, S. Golovato, R. Granetz, M. Greenwald, S. Horne, A. Hubbard, J. Irby, B. LaBombard, B. Lipschultz, E. Marmor, G. McCracken, M. Porkolab, J. Rice, J. Snipes, Y. Takase, J. Terry, S. Wolfe, C. Christensen, D. Garnier, M. Graf, T. Hsu, T. Luke, M. May, A. Niemczewski, G. Tinios, J. Schachter, and J. Urbahn, *Phys. Plasmas* **1**, 1511, (1994).
- ²B. Lipschultz, B. LaBombard, G. M. McCracken, J. Goetz, J. L. Terry, D. Jablonski, C. Kurz, A. Niemczewski, J. Snipes, *Proceedings of the 11th International Conference on Plasma Surface Interactions in Controlled Fusion Devices*, Mito, 1994, to be published in *J. Nucl. Mat.*
- ³G.F. Matthews, S.J. Fielding, G.M. McCracken, C.S. Pitcher, P.C. Stangeby, and M. Ulrickson, *Plasma Phys. Control. Fusion* **32**, 1301 (1990).
- ⁴R.S. Granetz, I.H. Hutchinson, J. Gerolamo, W. Pina, and C. Tsui, *Rev. Sci. Instrum.* **61** 2967 (1990).
- ⁵L.L. Lao, H. St. John, R.D. Stambaugh, A.G. Kellman, W. Pfeiffer, *Nucl. Fusion* **25** 1611 (1985).
- ⁶J.A. Goetz, B. Lipschultz, M.A. Graf, C. Kurz, R. Nachtrieb, J.A. Snipes, and J. L. Terry, *Proceedings of the 11th International Conference on*

Plasma Surface Interactions in Controlled Fusion Devices, Mito, 1994, to be published in J. Nucl. Mat.

⁷A. Niemczewski, B. Lipschultz, B. LaBombard, G. McCracken, *Proceedings of the 10th Topical High Temperature Diagnostics Conference*, Rochester, 1994, to be published in Rev. Sci. Instr.

⁸B. LaBombard, D. Jablonski, B. Lipschultz, G. McCracken, J. Goetz, *Proceedings of the 11th International Conference on Plasma Surface Interactions in Controlled Fusion Devices*, Mito, 1994, to be published in J. Nucl. Mat.

⁹G. Janeschitz, *Proceedings of the 11th International Conference on Plasma Surface Interactions in Controlled Fusion Devices*, Mito, 1994, to be published in J. Nucl. Mat.

¹⁰P.C. Stangeby, Nucl. Fusion **33** 1695 (1993).

¹¹Ph. Ghendrih, "Bifurcation to a Marfing Divertor Plasma Governed by Charge Exchange", submitted to Physics of Fluids.

¹²K. Borass and G. Janeschitz, submitted to Nuclear Fusion.

¹³J. Kesner, "Detached Scrape-off Layer Tokamak Plasmas", submitted to Physics of Plasmas.

¹⁴S.I. Krasheninnikov, D.J. Sigmar, T.K. Soboleva, P.J. Catto, "Thermal Bifurcation of SOL Plasma and Divertor Detachment", submitted to Physics of Plasmas.

Figure Captions

Fig. 1 - Cross-section of Alcator C-Mod showing divertor diagnostics and the diverted plasma equilibrium used for these studies.

Fig. 2 - Typical discharge conditions (shot#940623013) with data from probe diagnostics. Divertor detachment is observed after 0.82 seconds. Probe 6 is in the outer array.

Fig. 3 - Raw density and temperature profiles from the scanning probe. Profiles are characterized by smooth spline curves, shown here fitted to the data.

Fig. 4 - Density, temperature and pressure profiles in the SOL display clear non-exponential dependences on the cross-field coordinate which change as core density is varied.

Fig. 5 - Comparison of electron temperature and pressure profiles 'upstream' and at the divertor plate for three values of \bar{n}_e .

Fig. 6 - Evolution of density, electron temperature, and pressure on the $\rho = 4$ mm flux surface as a function of \bar{n}_e . Solid points refer to conditions at the divertor plate. Open points are 'upstream' at the scanning probe location. Electron pressure at the divertor plate is multiplied by a factor of 2 to account for the sound speed flow there.

Fig. 7 - Local pressure e-folding length, λ_p , versus T_e at the scanning probe location. An inverse scaling of λ_p with T_e is expected from

the transport model. A curve proportional to $T^{-5/4}$ is shown for comparison.

Fig. 8 - Change in key SOL and divertor plasma conditions with \bar{n}_e as the divertor approaches and enters the detached state. Parallel heat flux into the divertor is computed from the upstream electron temperature ($T^{7/2}$) using the transport model. Total divertor radiation seen by the bolometer diagnostic (including x-point region - see Fig.1) is normalized to total input power.

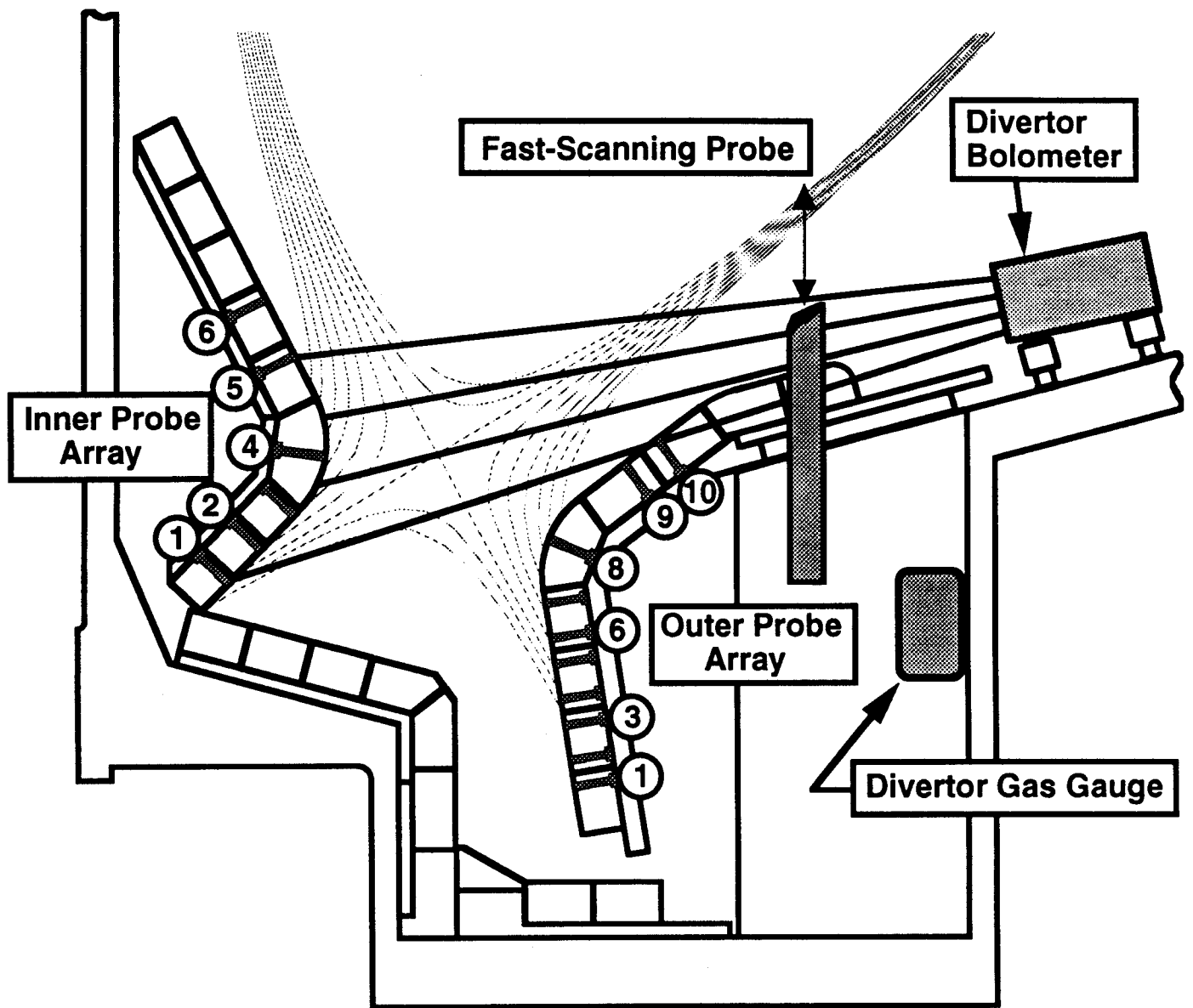


Figure 1

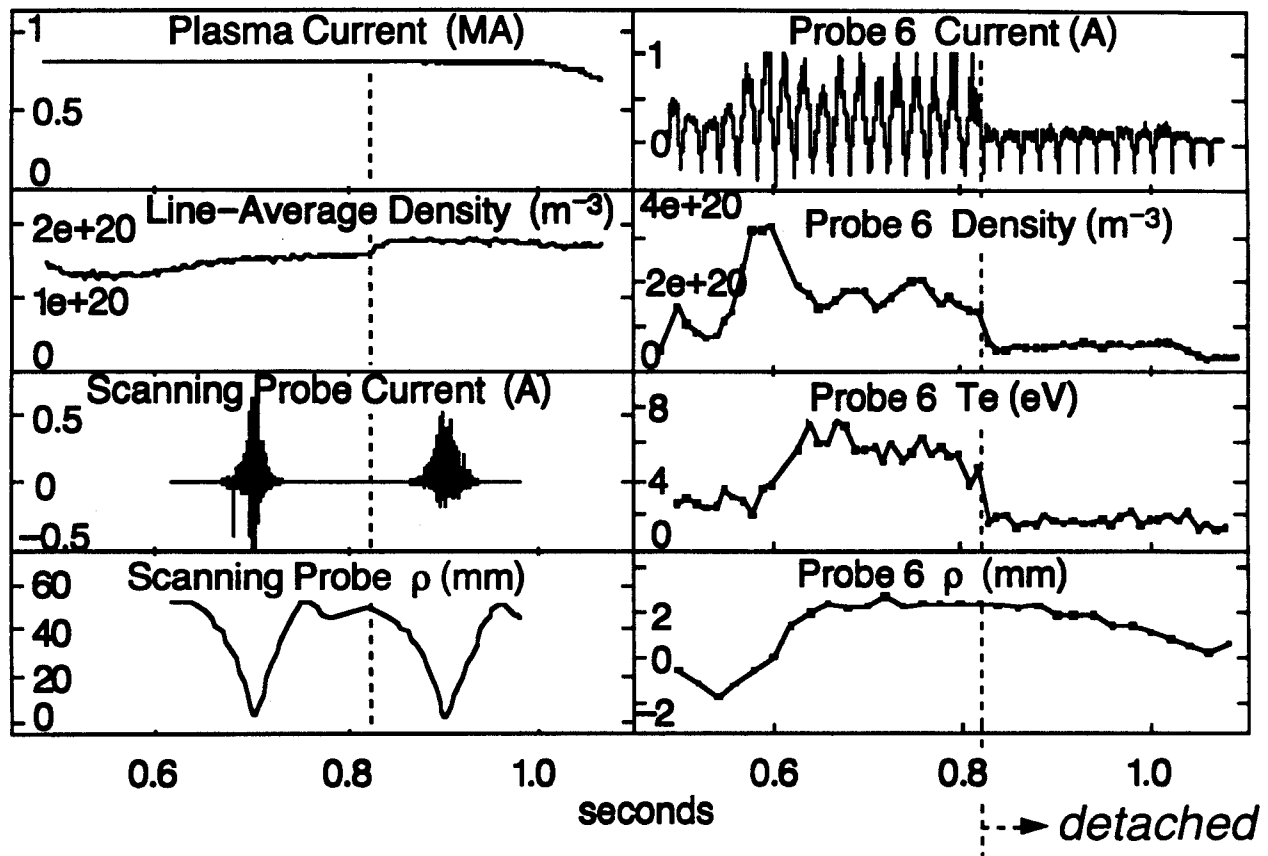


Figure 2

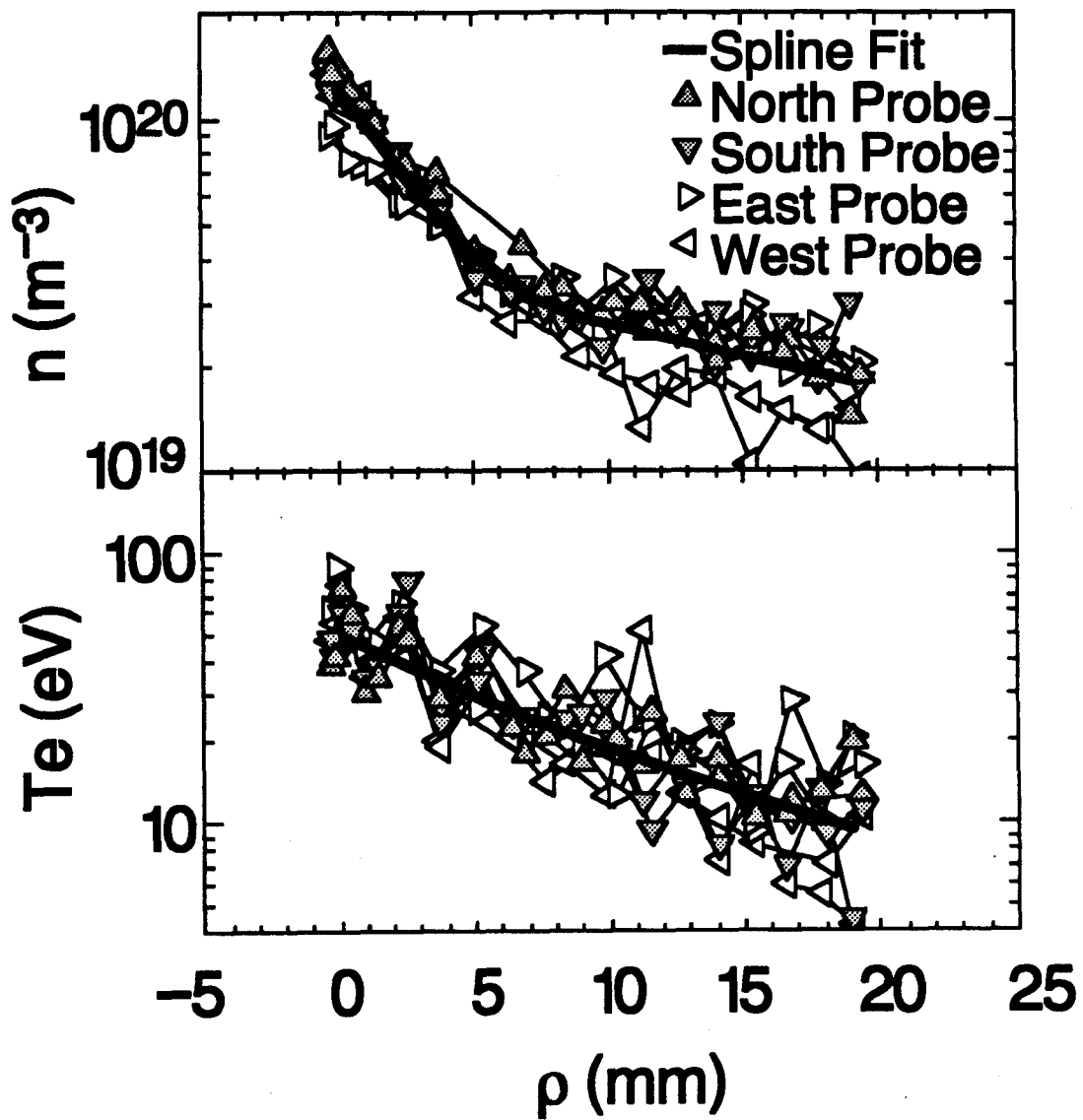


Figure 3

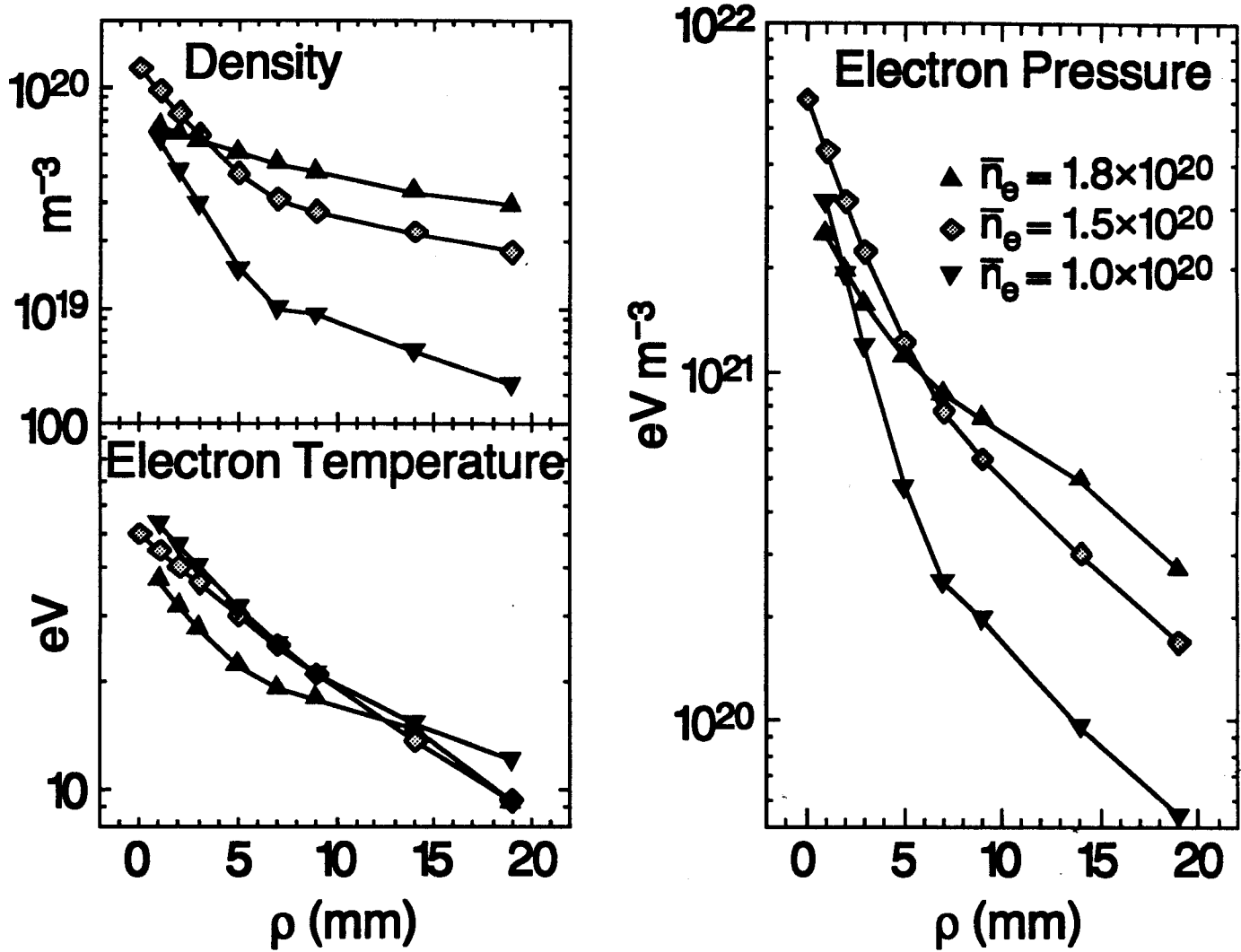


Figure 4

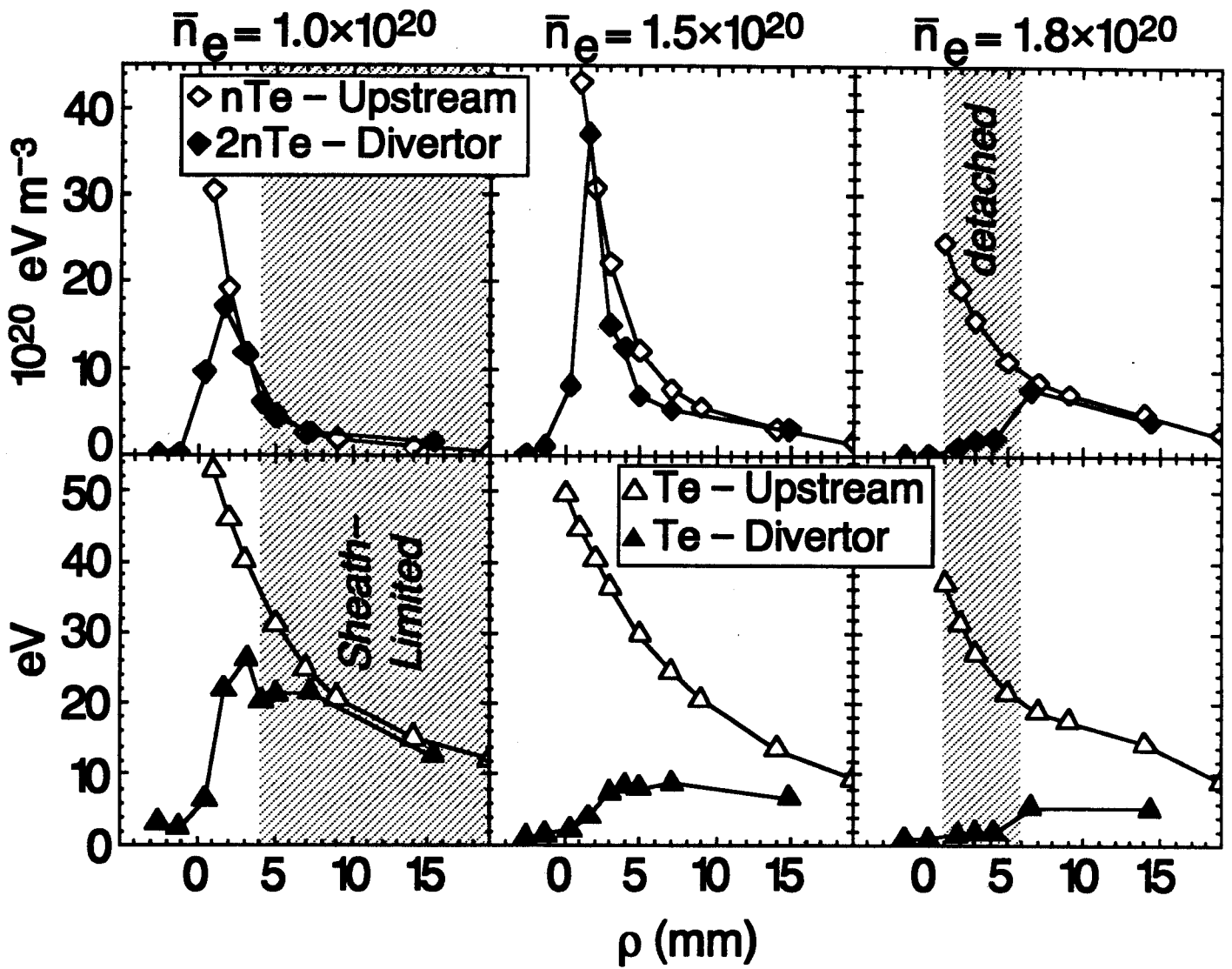


Figure 5

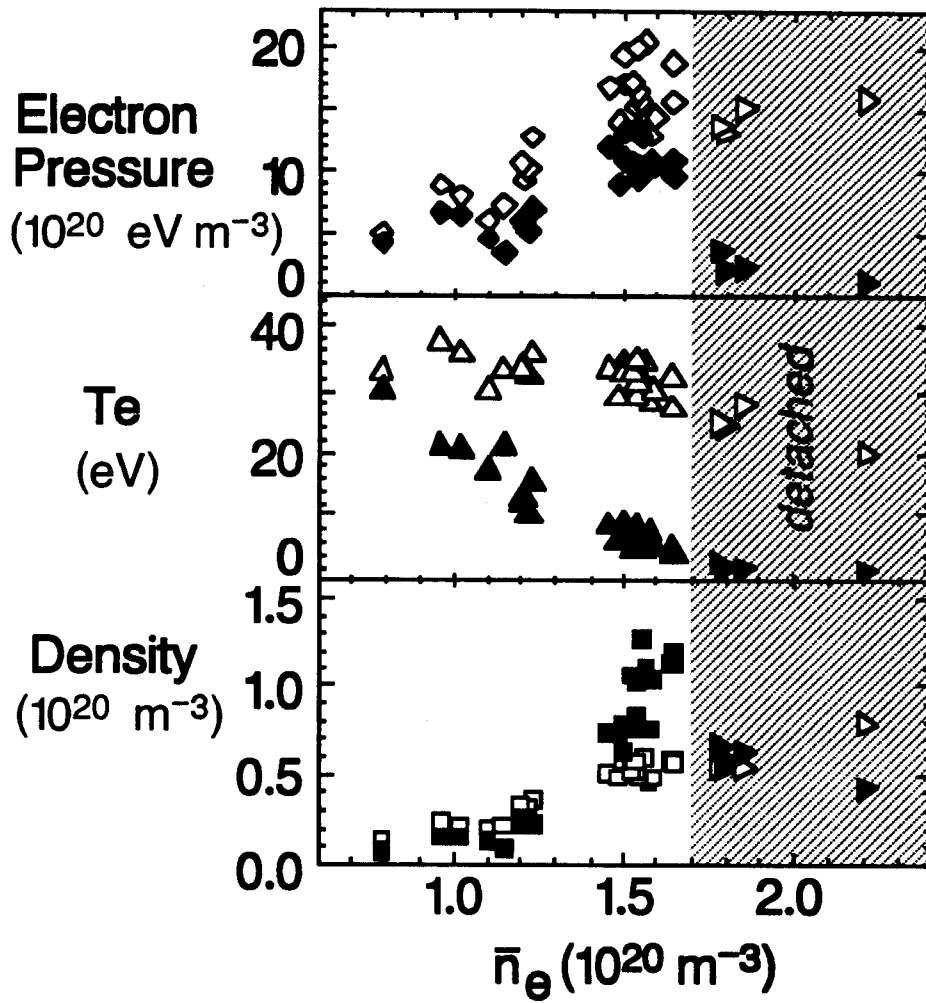


Figure 6

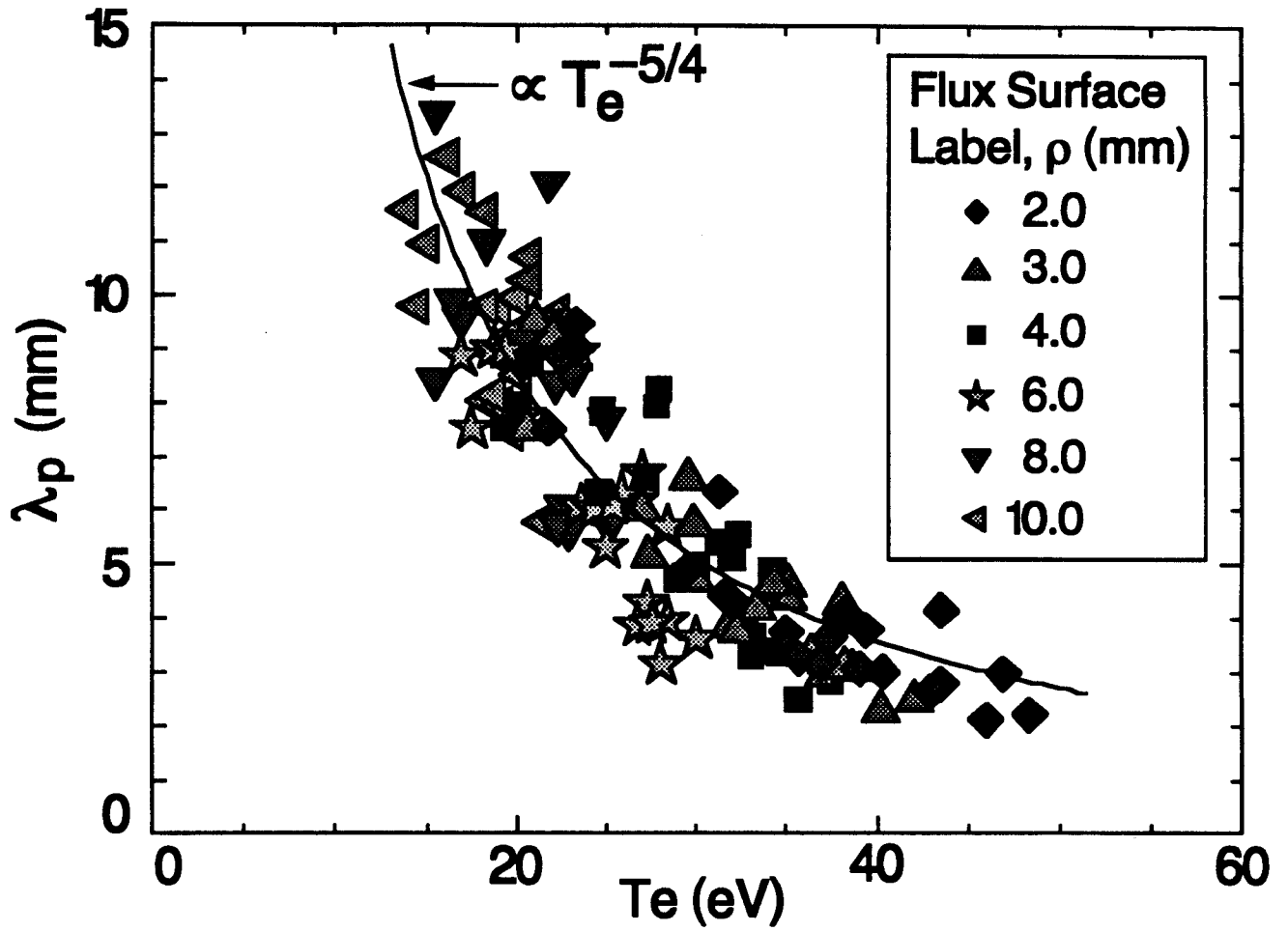


Figure 7

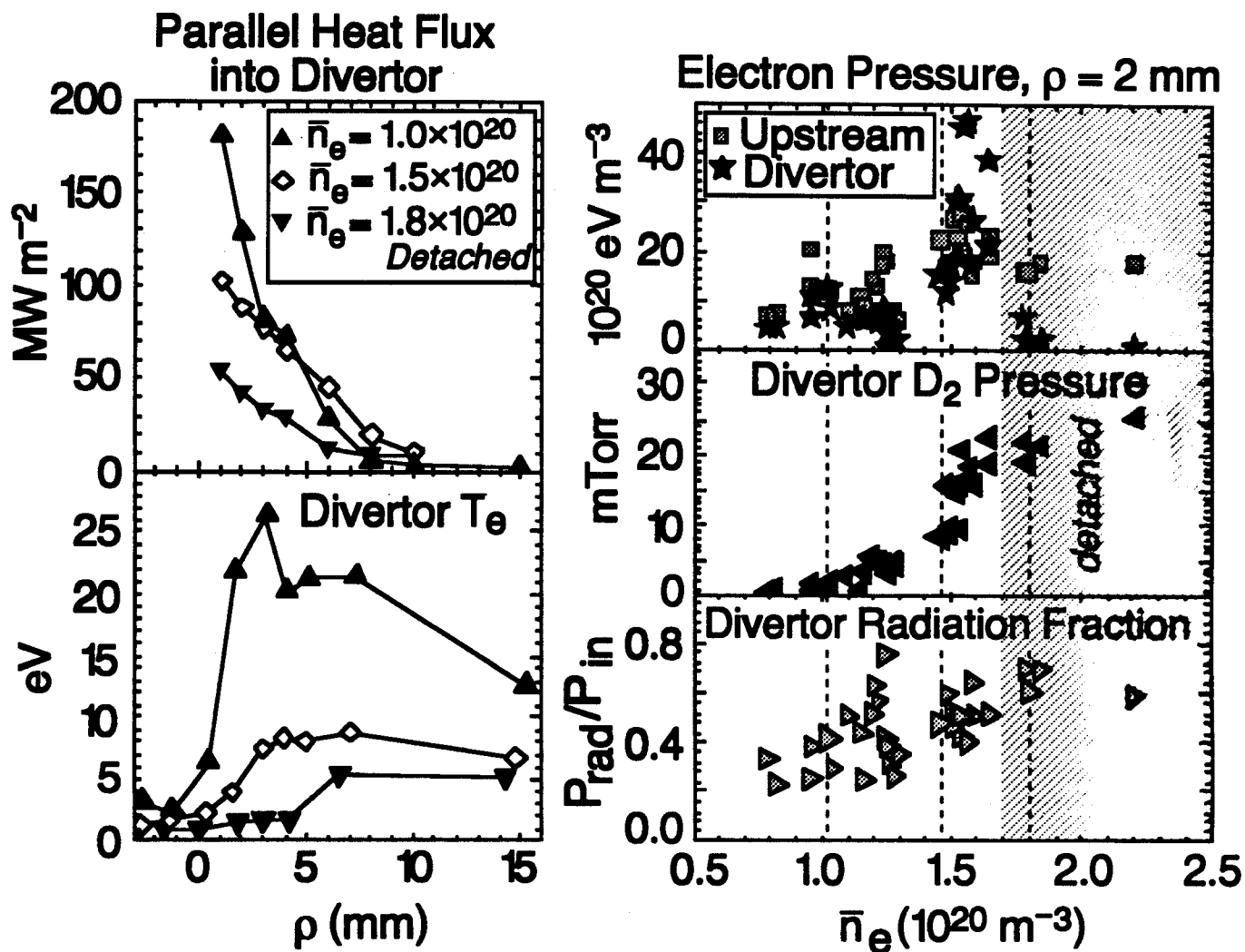


Figure 8

B. LaBombard, et al., "Scaling and Transport Analysis of Divertor"